



**HAL**  
open science

## Stellar mass spectrum within massive collapsing clumps

Yueh-Ning Lee, Patrick Hennebelle

► **To cite this version:**

Yueh-Ning Lee, Patrick Hennebelle. Stellar mass spectrum within massive collapsing clumps: III. Effects of temperature and magnetic field. *Astronomy and Astrophysics - A&A*, 2019, 622, pp.A125. 10.1051/0004-6361/201834428 . hal-03021444

**HAL Id: hal-03021444**

**<https://hal.science/hal-03021444>**

Submitted on 24 Nov 2020

**HAL** is a multi-disciplinary open access archive for the deposit and dissemination of scientific research documents, whether they are published or not. The documents may come from teaching and research institutions in France or abroad, or from public or private research centers.

L'archive ouverte pluridisciplinaire **HAL**, est destinée au dépôt et à la diffusion de documents scientifiques de niveau recherche, publiés ou non, émanant des établissements d'enseignement et de recherche français ou étrangers, des laboratoires publics ou privés.

# Stellar mass spectrum within massive collapsing clumps

## III. Effects of temperature and magnetic field

Yueh-Ning Lee (李悦宁)<sup>1,2,3</sup> and Patrick Hennebelle<sup>2,3,4</sup>

<sup>1</sup> Institut de Physique du Globe de Paris, Sorbonne Paris Cité, Université Paris Diderot, UMR 7154 CNRS, 75005 Paris, France  
e-mail: ynlee@ipgp.fr

<sup>2</sup> Université Paris Diderot, AIM, Sorbonne Paris Cité, CEA, CNRS, 91191 Gif-sur-Yvette, France

<sup>3</sup> IRFU, CEA, Université Paris-Saclay, 91191 Gif-sur-Yvette, France

<sup>4</sup> LERMA (UMR CNRS 8112), Ecole Normale Supérieure, 75231 Paris Cedex, France  
e-mail: patrick.hennebelle@lra.ens.fr

Received 15 October 2018 / Accepted 13 December 2018

### ABSTRACT

**Context.** The stellar mass spectrum is an important property of the stellar cluster and a fundamental quantity to understand our Universe. The fragmentation of diffuse molecular cloud into stars is subject to physical processes such as gravity, turbulence, thermal pressure, and magnetic field.

**Aims.** The final mass of a star is believed to be a combined outcome of a virially unstable reservoir and subsequent accretion. We aim to clarify the roles of different supporting energies, notably the thermal pressure and magnetic field, in determining the stellar mass.

**Methods.** Following our previous studies, we performed a series of numerical experiments of stellar cluster formation inside an isolated molecular clump. We investigated whether any characteristic mass is introduced into the fragmentation processes by changing the effective equation of state (EOS) of the diffuse gas, that is to say gas whose density is below the critical density at which dust becomes opaque to its radiation, and the strength of the magnetic field.

**Results.** The EOS of the diffuse gas, including the bulk temperature and polytropic index, does not significantly affect the shape of the stellar mass spectrum. The presence of magnetic field slightly modifies the shape of the mass spectrum only when extreme values are applied.

**Conclusions.** This study confirms that the peak of the initial mass function is primarily determined by the adiabatic high-density end of the EOS that mimics the radiation inside the high-density gas. Furthermore, the shape of the mass spectrum is mostly sensitive to the density PDF and the magnetic field likely only a secondary role. In particular, we stress that the Jeans mass at the mean cloud density and at the critical density are not responsible for setting the peak.

**Key words.** turbulence – ISM: kinematics and dynamics – stars: formation – stars: luminosity function, mass function – ISM: magnetic fields

## 1. Introduction

Deciphering the origin of the initial mass function (IMF), which describes the mass spectrum of stars at the moment of their birth (e.g., Kroupa 2001; Chabrier 2003; Bastian et al. 2010; Offner et al. 2014), is crucial for our understanding of the Universe since stars are the driving engine of the evolution of large structures. The stellar mass spectrum is the outcome of molecular cloud fragmentation, which is a process subject to the gravity and turbulence, as well as other physical factors such as thermal pressure, radiation, magnetic field, and stellar feedbacks. Observations over decades have suggested a relatively universal form of the IMF irrespective of the star-forming conditions, except for some recent works (Cappellari et al. 2012; Hosek et al. 2019) that have suggested possible variations. In particular, the IMF exhibits a characteristic peak at  $\sim 0.2\text{--}0.3 M_{\odot}$  with small variations observed exclusively in extreme environments. The high-mass end is usually described with a power law such that  $dN/d\log M \propto M^{\Gamma}$ , where  $\Gamma = -1.35$  typically (Salpeter 1955).

From the most classical point of view, the fragmentation of a medium is characterized by the Jeans instability criteria,

which is based on the density and temperature of the molecular cloud; other physical mechanisms such as radiation and magnetic fields probably play secondary roles. Simulations including more complete physics of the star formation, in particular the radiative transfer and stellar feedbacks, have been performed by many authors to explain the characteristic mass of the IMF (e.g., Bate et al. 2003; Bonnell et al. 2003; Offner et al. 2008; Girichidis et al. 2011; Krumholz et al. 2011; Ballesteros-Paredes et al. 2015), with theoretical models being developed in parallel (e.g., Padoan et al. 1997; Inutsuka 2001; Hennebelle & Chabrier 2008; Hopkins 2012). In this work, we focus particularly on the link between the characteristic value of the stellar mass spectrum from numerical simulations of molecular cloud collapse and the Jeans mass and magnetic Jeans mass of the initial cloud.

In previous studies, we examined the effects of initial cloud density and turbulent support, as well as numerical resolutions (Lee & Hennebelle 2018a, hereafter Paper I), and showed that the power-law slope at the high-mass end of the stellar mass spectrum depends on the relative importance of the turbulent, thermal, and gravitational energies. When the turbulent energy dominates over thermal energy, the fragmentation produces a

power-law mass distribution  $dN/d \log M \propto M^{-0.75}$ , while this distribution becomes flat otherwise. In particular by varying the mean density of the cloud by several orders of magnitude, we showed in Paper I that the mean Jeans mass within the cloud does not affect the peak position. We proposed a mechanism to explain the universality of the IMF peak (Lee & Hennebelle 2018b, hereafter Paper II), which is based on the mass of the first hydrostatic core (also called the first Larson core). The first Larson core defines the minimum mass required to trigger the second collapse that forms the protostar, and the tidal field around it prevents nearby fragmentation and thus leads to further mass accretion, yielding a final stellar mass that is about ten times that of the first Larson core. A more detailed statistical model was developed to account for this factor 10 (Hennebelle et al. 2018).

In this study, we consider other factors that may have an impact on the cloud fragmentation, notably the temperature and magnetic field. The thermal and magnetic energies act against self-gravity and could provide a characteristic scale for the fragmentation. The goal of this current study is to determine whether such characteristic scale does exist and is reflected in the mass spectra from cluster formation simulations. In contrast to what is intuitively expected, the peak of the stellar mass spectrum resulting from this study does not depend on the Jeans mass taken either at the mean cloud density or at the critical density. We confirm the results from Paper II that the characteristic mass is solely from the first hydrostatic core, i.e., the high-density part of the effective equation of state (EOS), and surrounding collapsing envelope.

The outline of this paper is as follows: In Sect. 2, the simulation setups are described in detail. The EOS of the gas and the magnetic field strength are varied. Sink particles are used to trace the formation and accretion of stars. In Sect. 3, the stellar mass spectra resulting from the simulations are presented and commented qualitatively. In Sect. 4, the effects of the varied parameters are discussed and interpreted more quantitatively. Finally, Sect. 5 concludes the paper.

## 2. Numerical simulations

### 2.1. The temperature

The thermal energy is one of the major supports against the gravity at prestellar core scales. We designed a series of simulations to investigate the effects of thermal behaviors at low densities on the gas fragmentation outcome. A barotropic EOS prescription is used for the temperature such that

$$T(n) = T_0 \left[ \left( \frac{n}{n_{\text{ad}}} \right)^{\gamma_0 - 1} + \left( \frac{n}{n_{\text{ad}}} \right)^{\gamma - 1} \right], \quad (1)$$

where  $T_0$  is the temperature of the diffuse bulk gas,  $n$  is the gas number density,  $n_{\text{ad}}$  is the critical density at which the gas turns adiabatic, and  $\gamma_0$  and  $\gamma$  are the polytropic indices for the diffuse and dense gas, respectively. Two effects are considered: first  $T_0$  is varied and secondly a shallow polytropic index  $\gamma_0$  other than 1 at low densities is considered. As suggested by previous studies that isothermal gas has no lower mass limit for fragmentation (Paper I; Guszejnov et al. 2018) and an adiabatic EOS (with  $\gamma \geq 4/3$ ) is necessary to yield a characteristic mass. We would like to verify that the low-density part of the EOS, that is to say below the critical density at which the gas becomes adiabatic, indeed plays no major role.

The classical expression for the Jeans mass is given by

$$\begin{aligned} M_J &= \frac{\pi}{6} \frac{c_s^3}{\sqrt{G^3 \rho}} = \frac{\pi}{6} \left( \frac{k_B}{\mu m_p G} \right)^{3/2} \rho^{-1/2} T^{3/2} \\ &= 5.1 \times 10^{-4} M_\odot \left( \frac{n}{10^{10} \text{ cm}^{-3}} \right)^{-1/2} \left( \frac{T}{10 \text{ K}} \right)^{3/2}, \end{aligned} \quad (2)$$

where the Jeans mass is defined as the mass contained in a sphere of diameter that is equal to the Jeans length,  $\rho = n\mu m_p$  is the density,  $T$  is the temperature,  $k_B$  is the Boltzmann constant,  $\mu = 2.33$  is the mean molecular weight,  $m_p$  is the proton mass, and  $G$  is the gravitational constant. For the EOS as suggested by Eq. (1) with  $\gamma_0 = 1$ , the Jeans mass decreases as  $n^{-0.5}$  at low densities and increases as  $n^{0.5}$  above the critical density of adiabatic heating,  $n_{\text{ad}}$ . The Jeans mass around  $n_{\text{ad}}$  has been traditionally considered to set the minimum mass for fragmentation and the question arises as to whether it may also set the peak of the IMF. On the contrary the argument proposed in Paper II only invokes the mass of the first hydrostatic core and is independent of Eq. (2).

With a view to test this argument for characteristic fragmentation mass based on the Jeans mass, we vary the EOS behavior in the low-density regime in a series of simulations. The run C from Paper I is taken as a reference. The initial cloud has  $M = 1000 M_\odot$  and is spherical with a density profile  $\rho(r) = \rho_0 / [1 + (r/r_0)^2]$ , where  $r$  is the distance to the cloud center and  $\rho_0$  and  $r_0$  are the density and size of the central plateau, respectively. The density contrast between the cloud center and edge is set to ten, and the radius consequently is  $3r_0$ . The simulation box size is twice the cloud diameter and the rest of the space is patched with a uniform diffuse medium of  $\rho_0/100$ . The turbulence is initially seeded with a Kolmogorov spectrum with random phases and no turbulence driving is employed. The amplitude of the turbulence is scaled to match the assigned Mach number.

#### 2.1.1. Bulk temperature of the diffuse gas

To investigate the effect of cloud overall temperature on the characteristic fragmentation mass, we performed a series of simulations with varied bulk temperature,  $T_0$ , while keeping  $\gamma_0 = 1$  in Eq. (1). This implies that the gas is isothermal at low densities, and heats up adiabatically owing to the dust opacity at higher densities with  $\gamma = 1.66$ , which is a reasonable approximation of the ISM up to the temperature of hydrogen molecule dissociation. We recall that in Paper II, the high-density end of the EOS was varied. More precisely, we studied different values of  $n_{\text{ad}}$  and  $\gamma$  and found a dependence of the mass spectra peak mass on the mass of the first hydrostatic core.

The simulations in Papers I and II had  $T_0$  fixed to 10 K. In this study, values of 40 and 100 K are used instead while keeping all the other parameters identical. The critical density  $n_{\text{ad}} = 10^{10} \text{ cm}^{-3}$  in the canonical run. For the other runs,  $n_{\text{ad}}$  is chosen such that the upper end of the EOS coincides with the canonical EOS (see Fig. 1), giving

$$n_{\text{ad}} = 10^{10} \text{ cm}^{-3} (T_0/10 \text{ K})^{1/(\gamma-1)}. \quad (3)$$

This choice ensures that the mass of the first hydrostatic core is unchanged while the Jeans mass at the critical density varies (see discussion in Sect. 4.1.1).

The ratio of gravitational to thermal energy is kept constant, and thus clouds with higher temperature have higher initial density. The canonical run T10M0+ is taken from the model C in Paper I with the ratio of free-fall time to sound-crossing time

**Table 1.** Parameters for simulations with varied EOS.

Label	$T_0$ (K)	$n_0$ (cm $^{-3}$ )	$n_{\text{ad}}(10^{10}$ cm $^{-3}$ )	$n_{\text{sink}}(10^{10}$ cm $^{-3}$ )	$\gamma_0/\gamma$	$l_{\text{max}}$	Resolution (AU)
T10M0+	10	$6.0 \times 10^7$	1	1	1/1.66	15	2
T40	40	$2.8 \times 10^9$	8.17	30	1/1.66	12	4
T100	100	$6.0 \times 10^{10}$	32.7	30	1/1.66	11	3
T10G12	10	$6.0 \times 10^7$	1	1	1.2/1.66	14	4
T10G07	10	$6.0 \times 10^7$	1	1	0.7/1.66	14	4

**Notes.** The label of the run, bulk temperature, cloud central density, adiabatic critical density, sink density threshold, polytropic indices, maximal refinement level, and physical resolution are listed.

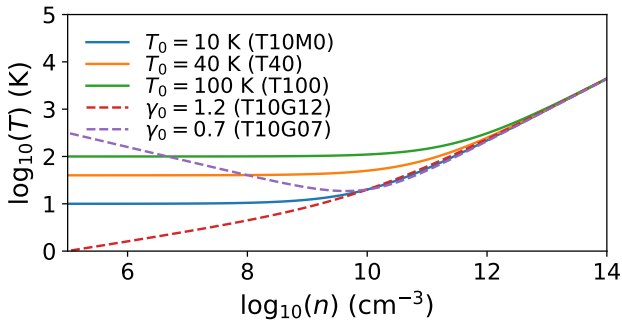


**Fig. 1.** Equation of state plotted in temperature as a function of gas number density, as listed in Table 1. Either the isothermal bulk temperature,  $T_0$  (solid curves), or the polytropic index,  $\gamma_0$  (dashed curves), is varied. The varied parameter and the corresponding run label are shown in the legend. With the purpose to understand the effects of temperature in low-density gas on the fragmentation outcome, the high-density end of all EOS is chosen to coincide.

$t_{\text{ff}}/t_{\text{sct}} = 0.05$ . The clouds are around virial equilibrium with the ratio of free-fall time to turbulence-crossing time  $t_{\text{ff}}/t_{\text{vct}} = 1.1$ . The numerical resolution  $l_{\text{max}}$ , which specifies the smallest cells size,  $1/2^{l_{\text{max}}}$  of the total simulation box, is chosen to have reasonably comparable physical resolutions. Higher density threshold of  $n_{\text{sink}} = 3 \times 10^{11}$  cm $^{-3}$  instead of  $10^{10}$  is used for sink particle formation to avoid artificial collapse before the gas reaches the adiabatic part of the EOS. This is necessary for the high temperature runs, while we demonstrated in Paper I that varying  $n_{\text{sink}}$  does not significantly affect the stellar mass spectrum. The parameters are listed in Table 1.

### 2.1.2. Polytropic index of the diffuse gas

The diffuse ISM is often reasonably approximated by an isothermal gas. In this study, we introduced a small dependence on the density with the polytropic index  $\gamma_0$  for the diffuse gas. The values of  $T_0 = 10$  K and  $\gamma = 1.66$  are used, and the canonical run has  $\gamma_0 = 1$  by construction. We performed two runs with  $\gamma_0 = 1.2$  and  $0.7$ , respectively. The parameters are also listed in Table 1.

The more diffuse gas is linked to the formation of cores of higher masses. With these setups, we aim to investigate whether different  $\gamma_0$  values have an impact on the distribution of the diffuse gas, and consequently affect the high-mass end of the stellar mass spectrum.

The EOS applied in simulations of this section are presented in Fig. 1. Either the isothermal bulk temperature or the polytropic index at low densities is varied, while the high-density end of all EOS is identical.

### 2.2. Magnetic field

The role of magnetic field during the fragmentation is also studied. The magnetic field provides extra support aside from the thermal pressure and turbulence, while also introducing some anisotropy. We varied the initial magnetic field strength to study the influences on the mass spectrum.

With respect to the canonical run T10M0+, a magnetic field is added at several strengths while keeping all the other parameters identical. The simulation is evolved following ideal magnetohydrodynamic (MHD) equations. We also perform a magnetized run with respect to the case A (here labeled T10M0A+) from Paper I, which has a lower initial density and higher thermal to turbulent energy ratio. The parameters are listed in Table 2.

### 2.3. Sink particles

Sink particles are used to follow the high-density self-gravitating regions below the resolution limit (Bleuler & Teysier 2014). The sinks are formed at the highest level of refinement when the local density maximum exceeds the prescribed threshold,  $n_{\text{sink}}$ , and the local gas is virially bound with converging flow. At the resolution of a few AU, it is guaranteed that a sink particle reasonably represents an individual star. We refer to Paper I for more detailed description of the algorithm and studies of numerical convergence.

For simulations with higher  $T_0$ , a higher value of  $n_{\text{sink}}$  is used because  $n_{\text{ad}}$  is increased. This avoids spurious sink particles formation before the adiabatic temperature increase. Although the selection of  $n_{\text{sink}}$  is indeed slightly delicate, by varying the value of  $n_{\text{sink}}$ , we demonstrated in Paper II that this has no consequences to the characteristic mass of the mass spectrum.

## 3. Simulation results

### 3.1. Sink particle mass spectrum

The mass spectra of sink particles are shown in Fig. 2 for simulations with varied bulk temperature,  $T_0$ . The three panels from top to bottom show runs with  $T_0 = 10, 40$ , and  $100$  K. The mass spectra are plotted at times when  $20, 50, 100, 150, 200$ , and  $300 M_{\odot}$  are accreted, where applicable since some runs are more evolved than the others. The number of stars decreases with increasing  $T_0$ , and the run T100 formed a few more massive stars. This is probably because the global density in run T100 is higher. In consequence, the fluctuations reach the adiabatic branch of the EOS more easily, and small fragments form less abundantly. On the other hand, the overall shape of the mass spectrum does not seem to vary much from one simulation to

**Table 2.** Parameters for magnetized simulations.

Label	$t_{\text{ff}}/t_{\text{act}}$	$t_{\text{ff}}/t_{\text{sct}}$	$n_0$	$\beta$	$\mathcal{M}_A$	$l_{\text{max}}$	Resolution (AU)
T10M0+	0	0.05	$6.0 \times 10^7$	inf	inf	15	2
M01	0.1	0.05		0.5	11	14	4
M04	0.4	0.05		0.03	2.75	14	4
M08	0.8	0.05		0.008	1.375	14	4
M12	1.2	0.05		0.003	0.92	14	4
T10M0A+	0	0.15	$8.2 \times 10^4$	inf	inf	15	8
M04A	0.4	0.15		0.03	2.75	14	17

**Notes.** The label of the run, the ratio of free-fall time to Alfvén crossing time, ratio of free-fall time to sound-crossing time, central density, the plasma  $\beta$ , Alfvénic Mach number, maximal level of refinement, and physical resolution are listed.

another. The peak at  $\sim 0.1 M_{\odot}$  is almost unchanged for the three runs of Fig. 2.

Figure 3 shows the two runs with  $\gamma_0 = 1.2$  and 0.7. There is no remarkable difference with respect to the canonical run. We note slightly steeper high-mass end slope for the run T10G12 and a slightly shallower slope for T10G07 in the range  $0.1-1 M_{\odot}$ . We discuss this as a possible effect of different values of  $\gamma_0$  in Sect. 4.1.2.

Figure 4 shows mass spectra from simulations with varied initial magnetic field strength with respect to the canonical run T10B0+. From run M01, M04, to run M08, there seems to be a flattening around the mass spectra peak and a slight broadening of the whole spectrum. Nonetheless, despite this weak trend, the spectra are very similar. Run M04 is not shown for conciseness since the spectra are also similar. The most magnetized run, M12, shows different behavior with more pronounced peak and limited number of low-mass stars. This may originate from the highly anisotropic geometry that resulted from the strong magnetic field.

Figure 5 shows the run A from Paper I and a magnetized run at same density. As discussed in Paper I, the mass spectrum becomes almost flat when the initial thermal energy is relatively important compared to the turbulent energy (i.e., lower density). The introduction of a magnetic field makes the mass spectrum more noisy, possibly by making the collapsing flow anisotropic, and slightly more massive stars are formed while the number of low mass objects is reduced. Overall, we do not see obvious qualitative differences in the two runs.

### 3.2. Density PDF

The mass spectrum is closely linked to the probability density function (PDF) of the density since it tells how much gas is subject to local collapse at each critical mass. We show in Fig. 6 the volume-weighted density PDF of the simulations and discuss the effect of varying the parameters. The left panel shows runs that have the same initial density as the canonical run. The gas cools at low density for  $\gamma_0 = 1.2$  (T10G12) and this has no visible effects on the density PDF. On the other hand, the thermal pressure increases with decreasing density for  $\gamma_0 = 0.7$  (T10G07). This lowers the Mach number at fixed turbulence strength and the density PDF is thus narrower at the low-density end. As for the magnetized runs, the density PDF at low densities narrows with increasing magnetic field strength. This might be because of the magnetic tension that prevents the gas from expanding. At the same time the increased magnetic pressure also narrows the density PDF. The effect is most obvious with the run M12. Most importantly however, the high-density ends of these PDF do not differ much from one another, and this is the most relevant part

for the unvarying mass spectra. A power law is plotted for comparison and this high-density end slope is invariantly compatible with  $n^{-1.5}$ . In the presence of self-gravity-driven turbulence, a collapsing cloud naturally develops a power-law density profile (Murray & Chang 2015; Murray et al. 2017), and thus in turn a power-law density PDF.

## 4. Discussion: physical effects on the mass spectrum

### 4.1. Effect of varying the temperature

Two major effects from the thermal pressure are expected. First, the isothermal temperature provides a scale-independent support against self-gravity. Secondly, the thermal pressure also affects the gas density PDF, which in turn affects the number of dense fluctuations that are susceptible to collapse.

#### 4.1.1. Bulk temperature of the diffuse gas

Our simulations are inspired by this argument about thermally regulated fragmentation and aim to clarify the effect of the temperature. The Jeans mass at  $n_{\text{ad}}$  in the simulations is

$$\begin{aligned}
 M_{\text{J,crit}} &= 5.1 \times 10^{-4} M_{\odot} \left( \frac{n_{\text{ad}}}{10^{10} \text{ cm}^{-3}} \right)^{-1/2} \left( \frac{T_0}{10 \text{ K}} \right)^{3/2} \\
 &= 5.1 \times 10^{-4} M_{\odot} \left( \frac{T_0}{10 \text{ K}} \right)^{3/2-1/2/(\gamma-1)} \\
 &\propto T_0^{3/4}, \tag{4}
 \end{aligned}$$

where the second equality results from the  $n_{\text{ad}}$  dependence that we chose to coincide the high-density end of the EOS. If this critical Jeans mass is the quantity determining the IMF peak, we should then see the peak of the mass spectra from our simulations shifting almost linearly with  $T_0$ , that is, 0.00051, 0.0014, and  $0.0028 M_{\odot}$  for  $T_0 = 10, 40$ , and 100 K. On the contrary, the peak mass in our simulations is independent of  $T_0$  and situates at  $\sim 0.1 M_{\odot}$  (see Fig. 2), which is two orders of magnitude larger than the critical Jeans masses. As suggested in Paper II, the characteristic mass of the IMF is indeed determined by the high-density end of the EOS, which is identical in this set of simulations. The lack of variation of the peak mass confirms this result.

With the gas heating up adiabatically, the first Larson core, that is a pressure-supported hydrostatic core, forms and has a mass  $M_{\text{L}} \sim 0.02 M_{\odot}$ . In Paper II, we derived the mass of the first Larson core by simply integrating the hydrostatic equilibrium equations while imposing the density and flat profile at the center as boundary conditions. When using an adiabatic EOS and

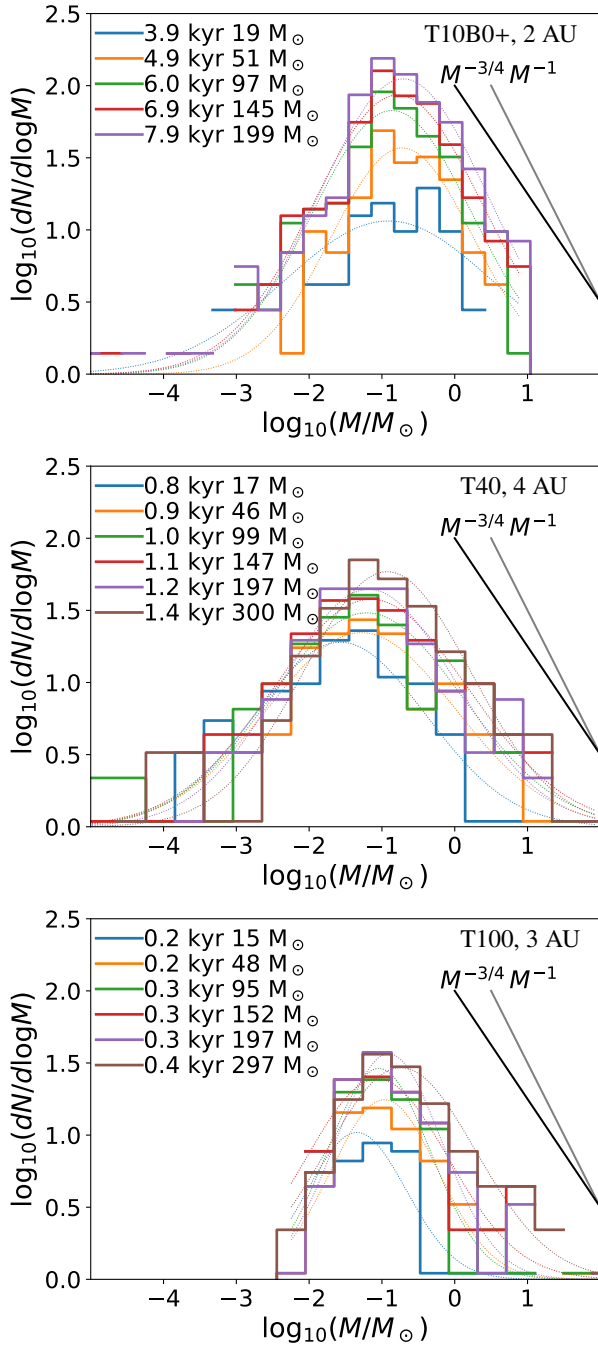


**Fig. 2.** Mass spectra with varying cloud bulk temperature. The colors blue, orange, green, red, purple, and brown represent the time at which about 20, 50, 100, 150, 200, and 300  $M_{\odot}$  have been accreted onto sink particles. Lognormal fits are shown with thin lines for reference. *Top panel:* canonical run T10M0+ (run C++ in Paper I), where the non-magnetized run has an EOS that sets the low-density gas to  $T_0 = 10$  K. *Middle panel:* (T40) with  $T_0 = 40$  K, similar peak position as the canonical run. *Bottom panel:* (T100) with  $T_0 = 100$  K, same characteristic peak mass, while the formation of low-mass sinks is clearly more difficult.

sufficiently high central density, the first Larson core is always well defined with a steep density drop at a few tens of AU. This density profile defines a mass that is not very sensitive to the central density. Such calculations give an idea of the typical mass of the first Larson core before the formation of the central singularity, the protostar.

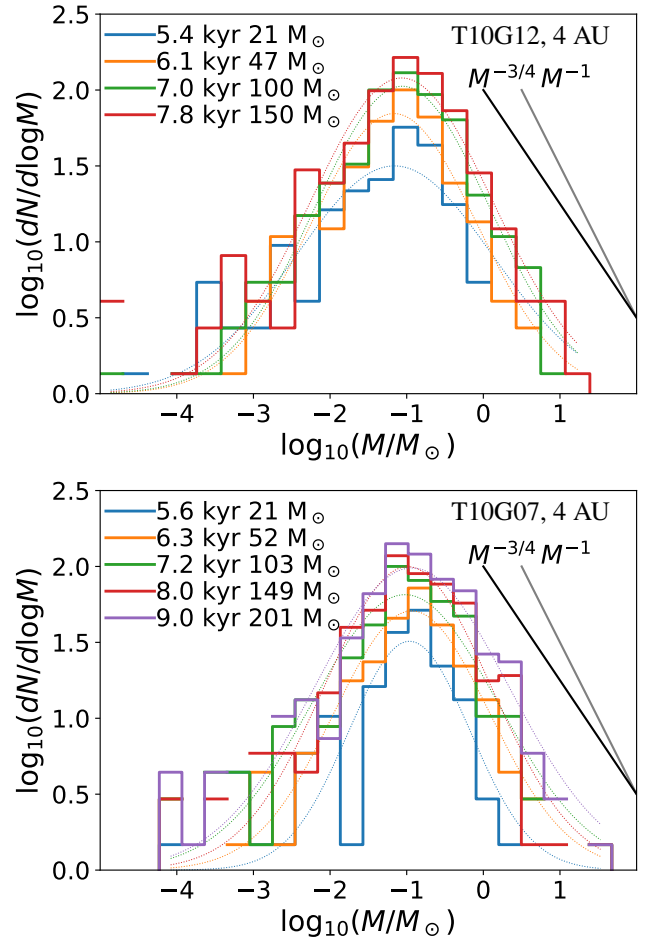


**Fig. 3.** Mass spectra with varying polytropic index  $\gamma_0$  at low densities, same color coding as in Fig. 2. Lognormal fits are shown with thin lines for reference. *Top panel:*  $\gamma_0 = 1.2$ ; *bottom panel:*  $\gamma_0 = 0.7$ . The mass spectra are very similar to those of the canonical run, and most importantly the peak position is not altered. The high-mass end slope of run T10G12 seems to be slightly steeper, and that of T10G07 shallower in the mass range from 0.1 to 1  $M_{\odot}$ .

We caution that the exact value of this mass depends on the detailed radiation-thermodynamics (Masunaga et al. 1998; Vaytet & Haugbølle 2017) and our treatment by a barotropic EOS is indeed very simplistic. The final mass of the star is determined by the competition between the fragmentation inside the surrounding envelope that tends to form new stars and block accretion and the tidal field of the star and envelope that tends to shear out density fluctuations and favor accretion. The result is a characteristic mass at  $\sim 10 M_L$  (Lee & Hennebelle 2018b; Hennebelle et al. 2018).

#### 4.1.2. Polytropic index of the diffuse gas

Following the previous discussions, it is already expected that the polytropic index of the diffuse gas,  $\gamma_0$ , in Eq. (1) has no obvious effects on the peak value of the mass spectrum. The density PDF, as already shown in Sect. 3.2, does not depend on  $\gamma_0$  at high densities. The power-law index with invariant value of  $-1.5$  is probably an outcome of the turbulent global collapse and independent of  $\gamma_0$ . We discuss the effect of  $\gamma_0$  in Appendix A if it were to be taken into account in the density PDF. Besides from this, we discuss the impact of  $\gamma_0$  in the thermally supported regime.

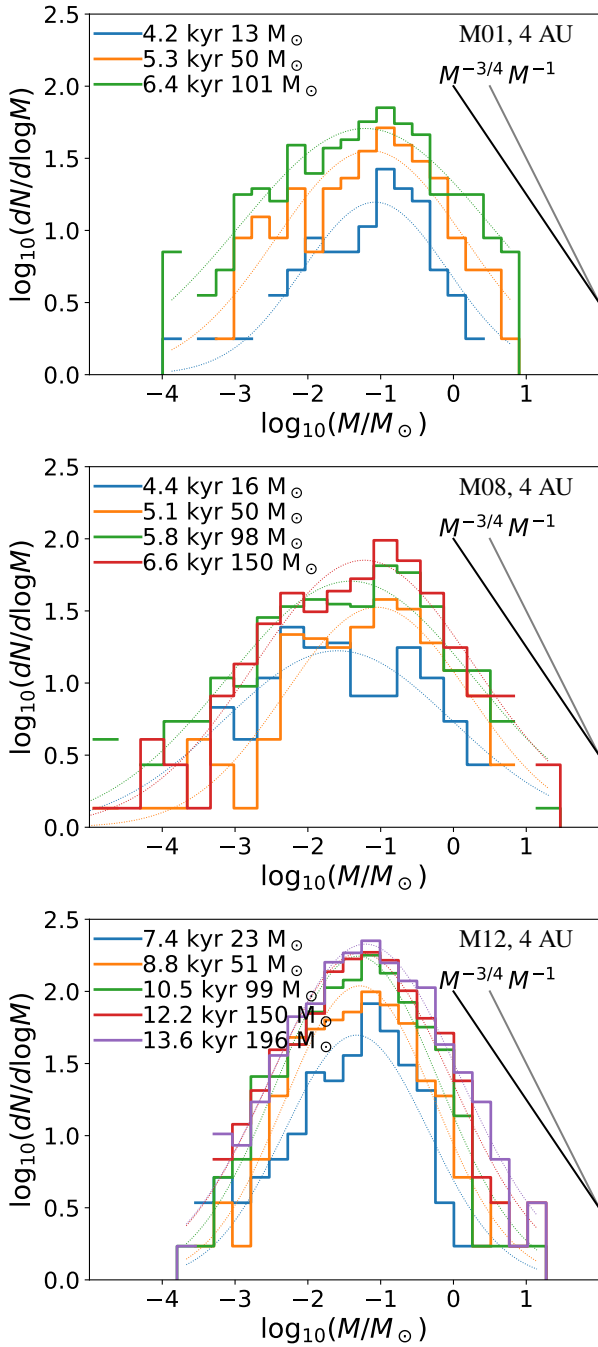


**Fig. 4.** Mass spectra with varying cloud magnetization, same color coding as in Fig. 2. Lognormal fits are shown with thin lines for reference. All runs have identical initial conditions as the canonical run except for the magnetic field strength that increases from top to bottom (M01, M08, and M12). The run M04 is not shown for conciseness since the spectra are not too different from either M01 or M08. The mass spectra are slightly broadened with respect to the nonmagnetized runs. Nonetheless, the magnetic field provides extra support without affecting the characteristic mass of cloud fragmentation in general. Only the most magnetized run (M12) with extreme field strength exhibits slightly different behavior probably from the anisotropic cloud collapse.

First as a reminder, the gravo-turbulent fragmentation model of the core mass function (CMF, [Hennebelle & Chabrier 2009](#)) was applied in Paper I to account for the power-law slope of the mass spectra while the density PDF is replaced by a power law. The virial equation of mass supported by dominating turbulent

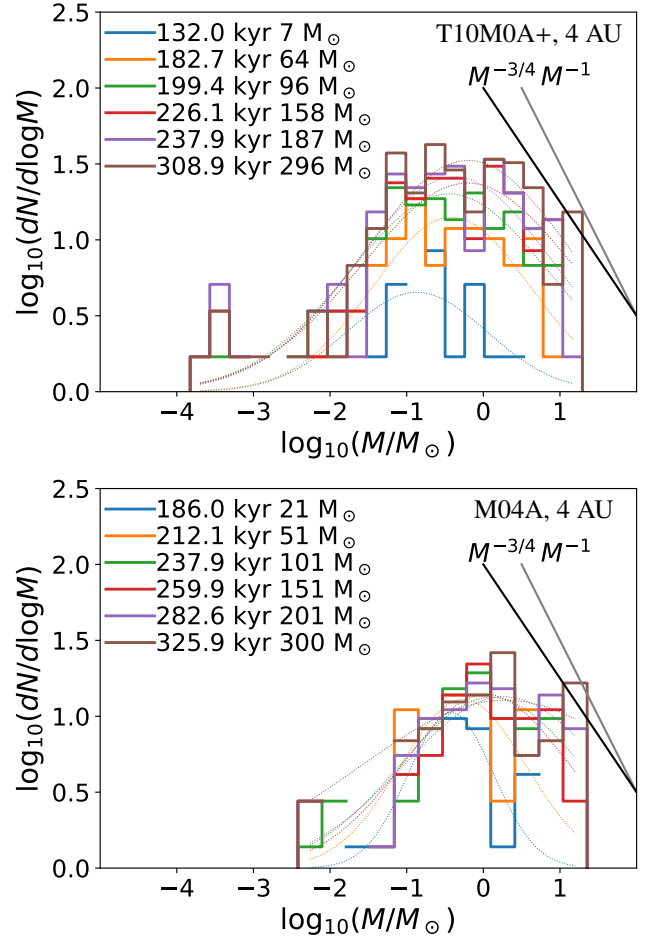


**Fig. 5.** Top panel: (T10M0A+) case A in Paper I, which has lower initial density compared to the canonical run. Same color coding as in Fig. 2 is used. Lognormal fits are shown with thin lines for reference. As explained in Paper I, the thermal support governs the mass fragmentations and the mass spectrum is almost flat. Introducing the magnetic field in the bottom panel (M04A) does not significantly change the overall behavior by adding extra support.

energy gives (Eq. (11) of Paper I)

$$M \propto R^{1+2\eta} \text{ and } \rho \propto M^{(2\eta-2)/(1+2\eta)}, \quad (5)$$

where  $R$  is the size of the self-gravitating structure and  $\eta = 0.5$  is the index of the turbulence power spectrum. Taking Eq. (2) from Paper I and density PDF  $\propto \rho^{-p}$ , we get the mass spectrum of self-gravitation structures as follows:

$$\frac{dN}{d \log M} = MN(M) \propto \frac{\rho}{M} \mathcal{P}(\rho) \propto M^{[-3+p(2-2\eta)]/(1+2\eta)}. \quad (6)$$

The mass spectrum has power-law index  $-3/4$  if  $p = 1.5$  is applied. We call this the TG regime (T and G for turbulent supported and global density PDF), which is what we see in most cases.

When the thermal support is dominant, then the mass-size relation from virial equilibrium becomes

$$M \propto R^{(4-3\gamma_0)/(2-\gamma_0)} \propto \rho^{(3\gamma_0-4)/2}, \quad (7)$$

which leads to

$$\frac{dN}{d \log M} \propto \frac{\rho}{M} \mathcal{P}(\rho) \propto M^{[2(p-1)+3\gamma_0-4]/(4-3\gamma_0)} \propto M^{-3(1-\gamma_0)/(4-3\gamma_0)}, \quad (8)$$

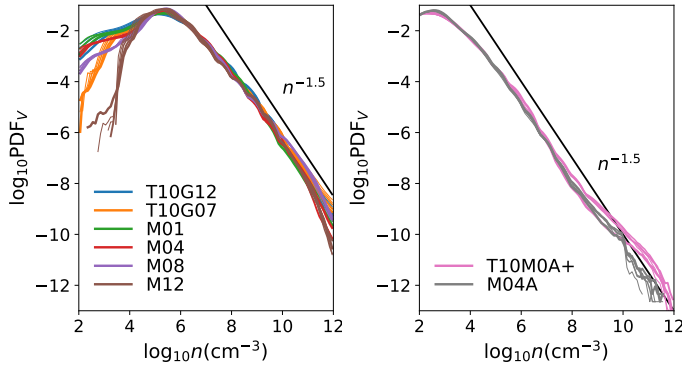


**Fig. 6.** *Left panel:* density PDFs for runs with varied  $\gamma_0$  and magnetization. The same time steps as used for the mass spectra are shown with decreasing line width. The density PDF is almost invariant in time. The high-density end merely changes from one run to another. A power law of  $n^{-1.5}$  is shown for comparison. The low-density end is narrower in run T10G07 because of the increasing thermal pressure with decreasing density. More magnetized runs have less low-density gas as well, due to similar effects. *Right panel:* density PDF of model A (lower initial density) without and with magnetic field. The magnetic field does not affect the PDF in the density range where stars are actively forming.

where the last result is obtained by applying  $p = 1.5$ . We call this the PG regime (P for pressure). The power-law index of the mass spectrum is 0 for  $\gamma_0 = 1$ , as already known from Paper I, and it becomes  $-0.47$  with  $\gamma_0 = 0.7$ . This is probably what we see in run T10G07 in the mass range between  $0.1$  and  $1 M_\odot$  with slightly shallower slope since the thermal support is stronger than that in the canonical run at low densities and the thermally supported regime emerges. The higher masses might reach the regime where the density PDF becomes lognormal and thus have a steeper slope.

Although from the density PDF and the model consistency it is mostly reasonable to use  $p = 1.5$  for the density PDF, we still do similar calculations for a local thermal density PDF in Appendix A for comparison (regimes TL and PL). The resulting power-law index of the mass spectrum is listed in Table 3 for the  $\gamma_0$  values in our runs. As a reminder, the discussed cases correspond to the density regime II in Paper I, where the gravity makes the density PDF a power law. The labels P and T correspond to support regimes a and b, correspondingly. The case of turbulent support combined with the global density PDF (TG) is simply the same as the TL case with  $\gamma_0 = 1$  since  $\gamma_0$  does not enter anywhere in the calculations. Meanwhile, the origin of this power-law index  $p = 1.5$  still remains to be further investigated.

#### 4.2. Impact of the magnetic field

Recalling from Paper I that the mass spectrum  $\mathcal{N}(M) = dN/d\log M \propto M^0$  when the thermal energy dominates over turbulence and  $\propto M^{-3/4}$  otherwise, the magnetic field seems to behave slightly similar to the thermal pressure. The mass spectra of the magnetized runs are wider with less remarkable peaks and show a slightly more flattened shape (between  $0.01$  and  $1 M_\odot$ ) than the nonmagnetized runs. Nonetheless, the variation among these runs are not very strong except for run M12, which has a very strong initial field. The whole cloud collapses along the field lines and has a more flattened geometry.

The statistics of the magnetic field strength are plotted against density for the four runs in Fig. 7. The runs M01, M04, M08, M12, and M04A are plotted in blue, orange, green, red,

**Table 3.** Power-law index of the mass spectrum in different model regimes.

$\gamma_0$	0.7	1	1.2
TG	–	$-0.75$	–
PG	$-0.47$	0	1.5
TL( $\eta = 0.5$ )	$-0.52$	$-0.75$	$-0.90$
PL	0	0	0

**Notes.** The labels indicate the supporting agent (turbulence/pressure) and the PDF (global/local).

and purple respectively. The lines with decreasing width correspond to the time steps where the sink mass spectra are shown in Fig. 4, and the shadows show the logarithmic standard deviation. The averaged magnetic field-density relation is almost invariant in time. With some dispersions, there is a clear trend of the field strength increasing with increasing density.

Three regimes are observed. We discuss these regimes using the relative importance of thermal (T), gravitational (G), and magnetic (B) energies. This is a simplified view since we only compare at global scales and real scale arguments are lacking. Various density dependences are plotted for reference.

- G>B>T: At low densities ( $<10^5 \text{ cm}^{-3}$ ) with weak magnetic field, the gravitational contraction proceeds isotropically without seeing the field. Simple magnetic flux freezing arguments lead to the relation  $B \propto n^{2/3}$  (Mestel 1965).
- B~G>T: At intermediate densities with strong field, the  $B$ - $n$  relation flattens. This corresponds to the regime where the field is strong enough to dominate the mass flow while the density is still too low to provide thermal support. The mass piles up along the field lines, and the density increases without increasing the magnetic flux. This regime only exists in runs with stronger initial fields (most clearly in M12).
- B~G~T: The high-density ends of the four runs almost coincide, and this possibly explains the very weak variation of the mass spectra. The thermally supported contraction along field lines at constant  $\beta = P_{\text{th}}/P_{\text{B}}$  leads to  $B \propto n^{1/2}$  (Mouschovias 1991). The exponent becomes 0.5 and 0.83 with  $\gamma = 1$  and 1.66 for density below and above  $10^{10} \text{ cm}^{-3}$ .

The behavior of the magnetic field is the outcome of the interplay between gravity, thermal pressure, and the field itself. The second regime is more clearly seen in run M12 with a strong initial field, and this implies an important anisotropy introduced by the presence of the magnetic field. The runs with weaker magnetic fields probably go directly from the first to the third regime.

Interestingly, when the thermal pressure becomes strong enough to support against the magnetically guided collapse at high densities in run M12, the field joins the  $B \propto n^{1/2}$  relation, but the field has a lower absolute value with respect to the other runs. This might be the reason for the different shape of mass spectrum of run M12, which is narrower with a rounder peak.

The averaged Alfvén velocity are also shown in Fig. 8 for reference, and basically the same behavior is seen. The Alfvén velocity of the four runs are all supersonic at densities below  $10^{10} \text{ cm}^{-3}$ . This is probably a necessary criterion for the magnetic field to have an impact on the mass spectra, and we basically do not see any effects with even weaker fields. On the contrary, the thermal support dominates over the magnetic field at high density, and this supports the lack of variation of the peak mass (Paper II).

In the regime where the initial density is low and where thermal support is relatively important with respect to the turbu-

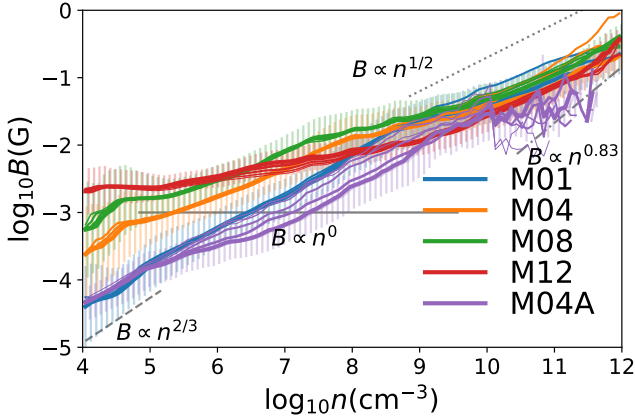


**Fig. 7.** Averaged magnetic field strength against density from runs M01, M04, M08, M12, and M04A in blue, orange, green, red, and purple. The same time step as in Fig. 4 and plotted with line width that decreases with increasing in time. Standard deviations are shown with shades. The relations  $B \propto n^{2/3}$  (dashed),  $B \propto n^0$  (plain),  $B \propto n^{1/2}$  (dotted), and  $B \propto n^{0.83}$  (dot-dashed) are plotted for reference.

lence, adding a moderate magnetic field (run M04A has the same plasma  $\beta$  as run M04) does not significantly change the mass spectrum except for possibly introducing more fluctuations. If we regard the magnetic pressure similar to the thermal pressure with some effective polytropic index for diffuse gas, this would result in  $\gamma_{0,\text{eff}} \sim 1$  if  $v_A \gtrsim c_s$  and  $\gamma_{0,\text{eff}} \sim 4/3$  otherwise. The second case is not important since the thermal pressure dominates, while in the first case the magnetic pressure behaves exactly like the thermal pressure and no significant difference should be expected.

To summarize briefly, the magnetic field reaches similar (subsonic) values at high densities irrespective of its initial value, and this is why the magnetic field does not play an important role in determining the characteristic mass of the molecular cloud fragmentation.

## 5. Conclusions

Following the previous study by Lee & Hennebelle (2018a,b), we enlarged the parameter space of our simulations by varying the thermal behavior of the diffuse gas and adding the magnetic field. We caution that this is a series of numerical experiments, of which the setup does not necessarily correspond to usual astrophysical conditions. Nonetheless, such choices of parameters allow us to systematically characterize the effect of certain physical mechanisms.

First of all, we varied the bulk temperature of the isothermal diffuse gas. The bulk temperature, together with the mean density, is classically believed to govern the characteristic fragmentation mass of a clump of diffuse gas. We already demonstrated previously that the adiabatic end of the EOS is the determining factor of the peak of the mass spectrum (Lee & Hennebelle 2018b). By varying the low-density end of the EOS, we confirmed that it is indeed the high-density end of the EOS that matters, not the transition point from the isothermal to adiabatic behavior.

Secondly, we varied the polytropic index of the low-density gas to replace the isothermal EOS. No effect was observed on the mass spectrum peak as expected. On the other hand, there seems to be a slight effect on the high-mass end of the mass spectrum due to a modification of the density PDF. We discussed such

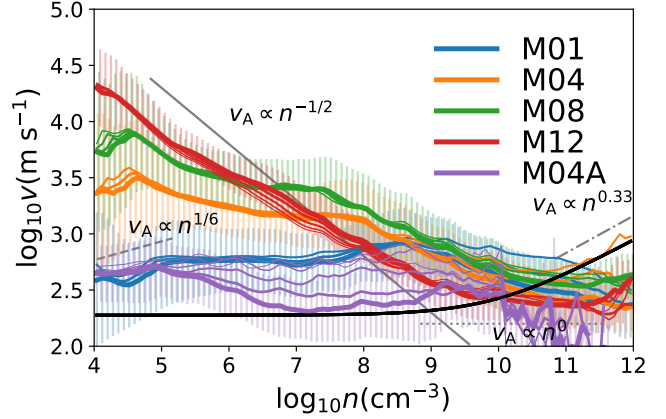


**Fig. 8.** Averaged Alfvén velocity against density from runs M01, M04, M08, M12, and M04A, in blue, orange, green, red, and purple. The same time step as in Fig. 4 and plotted with line width that decreases with increasing in time. Log standard deviations are shown with shades. The thermal sound speed is plotted in black for comparison. The relations  $v_A \propto n^{1/6}$  (dashed),  $v_A \propto n^{-1/2}$  (plain),  $v_A \propto n^0$  (dotted), and  $v_A \propto n^{0.33}$  (dot-dashed) are plotted for reference.

effect through simple arguments, while detailed studies of the density PDF behavior across scales remain to be better understood in the future.

Finally, we introduced magnetic fields at different strengths into two simulation setups with different initial densities, which correspond to models A and C in Paper I. We have shown that, despite of adding unphysically strong fields, the mass spectrum of the fragmentation results does not seem to be very much modified. Only the most magnetized case (M12) shows a more remarkable difference probably due to geometrical effects. In all circumstances, during local collapses, the magnetic field fails to reach high values that could provide significant support aside from the thermal pressure, and thus does not affect the characteristic mass of the fragmentation outcome. In physical conditions, the magnetic field unlikely plays an important role in terms of determining the mass distribution into fragments.

*Acknowledgements.* This work was granted access to HPC resources of CINES under the allocation x2014047023 made by GENCI (Grand Equipement National de Calcul Intensif). This research has received funding from the European Research Council under the European Community's Seventh Framework Programme (FP7/2007-2013 Grant Agreement no. 306483). Y.-N. Lee acknowledges the financial support of the UnivEarthS Labex program at Sorbonne Paris Cité (ANR-10-LABX-0023 and ANR-11-IDEX-0005-02)

## References

- Ballesteros-Paredes, J., Hartmann, L. W., Pérez-Goytia, N., & Kuznetsova, A. 2015, *MNRAS*, **452**, 566
- Bastian, N., Covey, K. R., & Meyer, M. R. 2010, *ARA&A*, **48**, 339
- Bate, M. R., Bonnell, I. A., & Bromm, V. 2003, *MNRAS*, **339**, 577
- Bleuler, A., & Teyssier, R. 2014, *MNRAS*, **445**, 4015
- Bonnell, I. A., Bate, M. R., & Vine, S. G. 2003, *MNRAS*, **343**, 413
- Cappellari, M., McDermid, R. M., Alatalo, K., et al. 2012, *Nature*, **484**, 485
- Chabrier, G. 2003, *PASP*, **115**, 763
- Girichidis, P., Federrath, C., Banerjee, R., & Klessen, R. S. 2011, *MNRAS*, **413**, 2741
- Guszejnov, D., Hopkins, P. F., Grudić, M. Y., Krumholz, M. R., & Federrath, C. 2018, *MNRAS*, **480**, 182
- Hennebelle, P., & Chabrier, G. 2008, *ApJ*, **684**, 395
- Hennebelle, P., & Chabrier, G. 2009, *ApJ*, **702**, 1428
- Hennebelle, P., Lee, Y. N., & Chabrier, G. 2018, *A&A*, submitted

Hopkins, P. F. 2012, *MNRAS*, **423**, 2037  
 Hosek, Jr., M. W., Lu, J. R., & Anderson, J., et al. 2019, *ApJ*, **870**, 44  
 Inutsuka, S.-I. 2001, *ApJ*, **559**, L149  
 Kroupa, P. 2001, *MNRAS*, **322**, 231  
 Krumholz, M. R., Klein, R. I., & McKee, C. F. 2011, *ApJ*, **740**, 74  
 Lee, Y.-N., & Hennebelle, P. 2018a, *A&A*, **611**, A88  
 Lee, Y.-N., & Hennebelle, P. 2018b, *A&A*, **611**, A89  
 Masunaga, H., Miyama, S. M., & Inutsuka, S.-I. 1998, *ApJ*, **495**, 346  
 Mestel, L. 1965, *QJRAS*, **6**, 161  
 Mouschovias, T. C. 1991, in *NATO Advanced Science Institutes (ASI) Series C*, eds. C. J. Lada, & N. D. Kylafis, 342, 61  
 Murray, N., & Chang, P. 2015, *ApJ*, **804**, 44  
 Murray, D. W., Chang, P., Murray, N. W., & Pittman, J. 2017, *MNRAS*, **465**, 1316  
 Offner, S. S. R., Klein, R. I., & McKee, C. F. 2008, *ApJ*, **686**, 1174  
 Offner, S. S. R., Clark, P. C., Hennebelle, P., et al. 2014, *Protostars and Planets VI*, 53  
 Padoan, P., Nordlund, A., & Jones, B. J. T. 1997, *MNRAS*, **288**, 145  
 Salpeter, E. E. 1955, *ApJ*, **121**, 161  
 Suto, Y., & Silk, J. 1988, *ApJ*, **326**, 527  
 Vaytet, N., & Haugbølle, T. 2017, *A&A*, **598**, A116  
 Yahil, A. 1983, *ApJ*, **265**, 1047

## Appendix A: Discussion on effect of $\gamma_0$

We discuss alternative models that consider the influences of  $\gamma_0$ . Using a value of  $\gamma_0$  other than 1 is expected to have effects both on the thermal Jeans mass and the density PDF. In the main article, we discussed a model where PDF is independent of  $\gamma_0$ , which is probably an outcome of a global turbulent collapse of the whole cloud (regimes TG and PG). In this work, we consider an alternative model, where  $\gamma_0$  affects the density PDF owing to local thermal equilibria.

With a polytropic index  $\gamma_0$ , the self-similar equilibrium solution yields a density profile (e.g., [Yahil 1983](#); [Suto & Silk 1988](#))

$$\rho \propto r^{-2/(2-\gamma_0)}. \quad (\text{A.1})$$

The volumetric density PDF is obtained by counting the volume at each density given that

$$\mathcal{P}(\rho)d\rho \propto 4\pi r^2 dr. \quad (\text{A.2})$$

Dividing each sides of Eq. (A.2) by  $d\rho$ , this then, after some manipulations, leads to

$$\mathcal{P}(\rho) \propto \rho^{(-6+3\gamma_0)/2} \propto \rho^{-p}, \quad (\text{A.3})$$

where  $p = 1.2, 1.5$ , and  $1.95$  for  $\gamma_0 = 1.2, 1$ , and  $0.7$ , respectively.

The power-law indices of the mass spectrum in the PG and PL regimes are obtained by simply inserting Eq. (A.3) into Eqs. ((6) and (8)). In the TL regime, the power-law index varies around  $-7.5$  for  $\gamma_0$  around 1 and stays negative for  $\gamma_0 < 4/3$ . In the PL regime, the effect of  $\gamma_0$  on the mass-size relation and on the PDF cancel out and the mass spectrum is flat in despite  $\gamma_0$ .

The behavior of run T10G07 is compatible with the slope of either the TL regime or the PG regime. In the TL case, the difference with respect to the canonical run results from the altered density PDF power law. In the PG case, this is explained by the movement of the sonic scale. Since the temperature is fixed at  $n_{\text{ad}}$ ,  $\gamma_0 < 1$  implies that the gas is hotter at low densities and therefore the turbulence becomes sonic at a larger scale. The pressure-supported regime is therefore extended to higher masses. The value  $\gamma_0 = 0.7$  with respect to 1, where  $n_{\text{ad}} = 10^{10}$  lowers the Mach number at the initial central density  $\sim 6 \times 10^7$  from 22 (see Paper I) to  $\sim 5$ , which means that the sonic point is not far from the mean density and the arguments of the TG regime seems to hold.